Failure Criteria of Unidirectional Carbon Fiber Reinforced Polymer Composites Informed by a Computational Micromechanics Model

Qingping Sun[a†], Guowei Zhou[b,c†], Zhaoxu Meng[d†], Haiding Guo[a], Zhangxing Chen[e], Haolong Liu[a], Hongtae Kang[f], Sinan Keten[d], Xuming Su[c]*

[a] Jiangsu Province Key Laboratory of Aerospace Power System, college of Energy and Power Engineering, Nanjing University of Aeronautics and Astronautics, Nanjing, China

[b] College of engineering, Ohio State University Columbus, OH 43212, USA

[c] Department of Materials Manufacturing, Ford Motor Company, Dearborn, MI 48124, USA

[d] Department of Civil and Environmental Engineering, Northwestern University, 2145 Sheridan Road, Evanston, IL 60208, USA

[e] State Key Laboratory of Mechanical Transmission, Chongqing University, Chongqing, China

[f] College of Engineering and Computer Science, University of Michigan-Dearborn, Dearborn, MI 48128, USA

† These authors contributed equally to this work.

* Corresponding authors:

ghd@nuaa.edu.cn (Haiding Guo)

Abstract

Failure prediction for carbon fiber reinforced polymer (CFRP) composites has been a longstanding challenge. In this study, we address this challenge by first applying a computational micromechanics model based on representative volume element (RVE) to predict the failure envelopes of unidirectional (UD) CFRP composites. Then, these failure envelopes are compared with the classical failure criteria. We have evaluated the performances of these failure criteria and identified the aspects for further improvement in their accuracies for the UD CFRP composites studied herein. Based on the failure mechanisms from computational results and the comparisons between predicted failure envelopes and classical failure criteria, a new set of homogenized failure criteria is proposed. The newly proposed failure criteria show significant improvement in the agreement with both our computational and experimental results. Furthermore, we have compared the proposed failure criteria with existing experimental data and computational results available in the literature for different types of composites. Good agreements between them are generally observed.

Keywords

Carbon fiber-reinforced polymer composites, Computational micromechanics model, Representative volume element, Failure criteria

1. Introduction

Carbon fiber reinforced polymer (CFRP) composites have numerous applications in lightweight structures in the aerospace and automotive industry, due to their excellent strength and stiffness. The fast-expanding demand for these composites requires efficient material characterization techniques to predict their mechanical properties, most notably their failure behaviors under various loading conditions for safety concerns. Different from most homogeneous materials that exhibit a limited number of physical failure mechanisms, of which it is easy to formulate theoretical failure criteria, i.e., the mathematical and/or phenomenological evaluation of the critical stresses that lead to the onset of damage [1], CFRP composites, with heterogeneous structures and interfaces between different phases, tend to present multiple failure modes depending on loading directions, stress states, and possible manufacturing defects [2]. In this case, the coexistence of various failure modes and failure mechanisms in CFRP composites implies the necessity to use different failure criteria depending on stress states. In addition, failure locus in the stress space usually locates at the intersection of various smooth surfaces, with each one representing the critical condition for a given fracture mode. Therefore, accurate and robust failure criteria to predict failure envelopes of CFRP composites subjected to multi-axial stress state are much more challenging, and it remains as a key aspect in the optimal design of a composite structure.

Over the years, numerous failure criteria have been proposed to describe the failure envelopes for CFRP composites from limited experimental data. Typical failure criteria have been successfully used in the analysis, design, and calculation of safety factors of composite structures subjected to complex loading and boundary conditions. They include but not limited to strain-based [3], stress-based [4-9], as well as their replacement of phenomenological failure criteria [10-15]. Recently, a set of fully three-dimensional failure criteria for fiber-reinforced composites have been proposed [16-18] and reviewed in the literature. Although many failure criteria have been proposed, validating them remains challenging. In addition, some recent efforts have

shown that the failure behaviors depend not only on the onset of failure predicted by the failure criteria, but also on the subsequent fracture propagation processes [19].

Due to the significant uncertainties in the validation of the failure criteria, many efforts have been devoted to comparing them with each other and with experimental data [17, 20]. In particular, the recent World-Wide-Failure Exercise (WWFE) conceived and conducted by Hinton and Soden [2, 21, 22] provides a good assessment of currently available failure criteria for predicting failure in carbon and glass fiber composites. WWFE showed that the predictions of many failure criteria differed significantly from the experimental results, particularly under multi-axial stress states involving matrix fracture and/or fiber compression. However, precise conclusions regarding which criterion best reproduces the physical failure mechanisms and the mechanical strength have not been reached due to the scarcity of experimental results under multi-axial stress states. Furthermore, there are several limitations for experimental tests because specific loading conditions or geometries of the test specimens are extremely difficult to obtain. Thus, many existing failure criteria for strength prediction have not been validated.

On the other hand, many of these difficulties can be overcome by virtual testing by means of computational micromechanics analysis. In particular, computational studies are advantageous in the systematic characterization of the effects of fiber and matrix properties and microstructures on the composites' mechanical response [23]. In addition, virtual experiments could avoid the complexity and variability of conditions in real tests, especially when complicated loading cases such as bi-axial or tri-axial loading tests are involved. Recently, computational analysis has been successfully employed to investigate the mechanical behavior of fiber-reinforced lamina up to failure subjected to different combined loading conditions [1, 24-29]. This approach provides full control of the constituent properties, spatial distribution, and loading, eliminating many sources of experimental error. Nevertheless, accurately modeling the inelastic and failure behavior of CFRP composites remains a difficult challenge due to various factors, such as (1) the high fiber volume fraction of the fibers leads to

stress or strain concentrations in the matrix; (2) the distinct properties of the interphase region between fiber and matrix also influence the inelastic and failure behavior of the composites [30]; (3) fiber distribution is non-uniform [30]; and (4) the manufacturing process introduces different defects (fiber shape [31, 32], fiber waviness [33], interface properties [34, 35], fiber-matrix interface defects [36], thermal residual stress [23, 34], micro-voids [29, 37]). These factors limit the applicability of computational models with homogenized behaviors of the composites or constituents.

In this paper, a computational micromechanics model based on representative volume element (RVE) modeling is developed to investigate the failure mechanisms and calibrate the failure envelopes of UD CFRP composites. This model addresses several challenges aforementioned. First, we consider the influence of the distinct interphase region on the failure behavior of the composites. Then, we accurately represent the fiber volume fraction according to experimental samples. Also, we adopt a fiber waviness function in the longitudinal direction to represent the defects introduced from the manufacturing process. This computational micromechanics model enables us to propose a new set of homogenized failure criteria for the UD CFRP composites. In detail, we first use the computational model to investigate the failure mechanisms and failure envelopes of the composites under combined transverse load and in-plane/out-of-plane shear, i.e., σ_{22}-τ_{12} and σ_{22}-τ_{23}. Afterwards, we further include local fiber waviness in the fiber longitudinal direction in our RVE model. It then enables us to consider the longitudinal deformation of the composites and predict the failure envelopes under combined longitudinal compression and in-plane shear, i.e., σ_{11}-τ_{12}. Then, the calibrated failure envelopes are compared with the predictions of the classical failure criteria. The results show that within $\sigma_{22}<0$ in σ_{22}-τ_{12} and σ_{22}-τ_{23} stress space, there are obvious differences between computational results and classical failure criteria, especially in the high shear stress regime. We have found out that it is because the transition in dominant failure mechanisms observed in computational results has not yet been considered in existing failure

criteria. Furthermore, most of the current failure criteria cannot match our computational failure envelope of σ_{11}-τ_{12}. To address the limitations of the current failure criteria, a new set of homogenized failure criteria of UD CFRP composites is proposed for predicting composite failure under multi-axial stress states. The proposed failure criteria are based on the failure envelopes and failure mechanisms observed from the computational micromechanics model. Finally, the accuracy of the proposed failure criteria is validated by comparing the analytical predictions with our computational and experimental results under multi-axial stress states. We have also compared our proposed failure criteria with other experimental or computational data found in the literature for different types of fiber-reinforced composites.

2. Computational micromechanics model

2.1. RVE model set-up

By adopting an algorithm proposed by Melro et al. [38], we generate the cross-section microstructure of our RVE model with cylindrical fibers randomly distributed in the matrix for high values of fiber volume fraction. In addition to the fiber and matrix phase, our RVE model also consists of a finite thickness (~200 nm) interphase region adjacent to the fibers. We use this interphase region to capture the unique properties of the transition zone between the carbon fiber and resin matrix, as described in our previous work [30]. A zero-thickness interface between fiber and interphase region is also considered to capture the realistic failure strength and debonding failure mechanism by inserting cohesive elements, as shown in Fig. 1. The fiber volume fraction within the RVE is about 51% in this study, which is the same as the experimental sample.

Apart from the selection of the RVE size, the applied boundary conditions play a key role in the assessment of mechanical properties. We would like to note that the RVE size and boundary conditions are actually closely related [39, 40], and a common practice is that the independence on the boundary condition is considered as the indicator for the sufficiency of the RVE size. The classical approach to introduce periodic boundary condition (PBC) in a RVE is by means of the definition of

constraint equations (*EQUATION in Abaqus [41]) between periodic nodes, hence imposing constrains to their allowed displacements. In its essence, this method requires the mesh to be periodic, in such a way that every node on each RVE boundary has its homologous node on the respective opposite boundary. The traditional PBC approach is well appropriate for standard [1, 25] and implicit integration numerical schemes, but exhibits several drawbacks when explicit dynamic time integration is used. It is observed that the relationships between master and slave displacement is translated into equations that introduce intense high-frequency oscillations in the system that compromise the numerical solution [42]. Moreover, the method with traditional PBC is computationally expensive. An alternative approach is to apply uniform boundary conditions (displacement or traction). It has been shown that for sufficiently large RVEs, the results obtained from using PBC are close to those obtained from using uniform boundary conditions [43-45]. Thus, in this work, loading is applied by imposing uniform displacements (traction) on the boundary nodes. To choose a sufficiently large RVE, we adopt the size convergence approach [39] in which the RVE size is gradually enlarged and we take the size where the results reach convergence. Previous study has shown that the results obtained with 30 fibers in the RVE were equivalent to those computed with 70 fibers in terms of the stress-strain curves and of the dominant failure micro-mechanisms when subjected to transverse compression and shear [1]. Following the previous research, we choose our RVE size to include around 50 fibers, and this size has been reported to be sufficient to capture the essential micro-scale features with relatively low computational costs [28, 46].

The RVE is developed using Abaqus/Explicit [41] in the following way: an orphan mesh technique with predominantly first-order hexahedral elements under reduced integration (C3D8R) and tetrahedral elements (C3D6) is adopted for these three phases, while first-order cohesive elements (COH3D8) are used to represent the interface. To generate a well-structured, high-quality mesh, a seed density of 2 elements in the thickness direction of the interphase region is used, leading to an average element size for the interphase region of 0.1 um, while the element size of

fiber and matrix are slightly larger with a size around 0.35 um. Mass scaling artificially increases the mass of elements. It is therefore essential to remain aware that adding some "nonphysical" mass to increase the time increment can strongly affect the results, especially for a dynamic study and the inertia effects could become dominant. A common technique to check a posteriori that the mass scaling does not significantly affect the results is the comparison between the kinetic energy and the internal energy of the system. This ratio is often chosen below 5–10% [47]. The mass scaling (stable time increment) 1e-5 is selected in this study. The linear bulk viscosity in Abaqus-explicit is set to be 0.06 and the quadratic bulk viscosity parameter is 1.2.

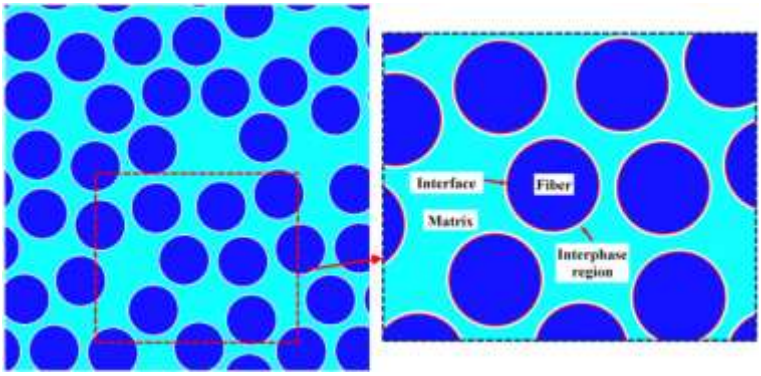

Figure 1. Schematic cross-section view of the microstructure of UD CFRP composites used in the RVE model.

2.2.Constitutive models of the three phases

In the RVE model, carbon fibers are assumed to be transversally isotropic and linearly elastic. The five independent material constants of AKSACA carbon fibers are listed in Table 1. The fiber diameter is 7 *um*. The fiber volume fraction is around 51.4%, consistent with the specimen used in experimental analyses.

The polymeric matrix of epoxy is modeled as an isotropic elasto-plastic solid and it follows the isotropic damage law proposed by Melro et al. [48], implemented as a VUMAT user subroutine. A paraboloidal yield criterion, defined as a function of the stress tensor and the compressive and tensile yield strength, is used together with a non-associative flow rule, which allows for a correct definition of the volumetric deformation in plasticity. Damage onset is defined by a damage activation function

similar to the paraboloidal yield criterion, but using the final compressive and tensile strengths of the epoxy matrix instead of yield strengths. The detailed constitutive model can be found in our previous study [30, 33].

We would like to note that the epoxy resin used in this study shows first softening and then re-hardening plastic deformation behaviors under compression at room temperature. Plastic softening for matrix inevitably causes some numerical difficulties for implicit FEA, although several techniques such as viscous damping [49] have been used to circumvent it to some extent. By comparison, a favorable approach is to resort to explicit FEA method [50] to perform microscopic progressive failure analysis of the CFRP composites. This further justifies our explicit approach.

As studied previously, the average properties of the interphase region have been calibrated based on molecular dynamics simulations on similar epoxy resins and an exponential gradient model as shown in our previous studies [30, 51]. The average Young's modulus and strength of the interphase region are found to be around 5 and 9 times larger than those of bulk resin matrix. The constitutive behavior and damage model of the interphase are assumed to be similar to those of the matrix model proposed earlier [30].

Interfacial debonding is considered by inserting cohesive elements at the interface between the fiber and interphase region, with a constitutive response defined by a bilinear mixed-mode softening law. Damage onset is predicted by a quadratic interaction criterion which depends on the interface strength for each damage modes. Once debonding is initiated, the cohesive tractions linearly decrease to zero. We also adopt the energy-based Benzeggath-Kenane (BK) damage propagation criterion to account for the dependence of the fracture energy dissipation on fracture modes [52]. The interfacial fracture strength and energy have been calibrated based on a reverse engineering method according to experimental tests [30]. The calibrated and validated cohesive parameters are also listed in Table 1.

Table 1. Model parameters in the RVE model

Carbon fiber	E_{11} (GPa)	E_{22}=E_{33} (GPa)		G_{12}=G_{13} (GPa)	G_{23} (GPa)	ν_{12}
	245	19.8		29.191	5.922	0.28
Epoxy matrix	E_m (GPa)	ν_m	ν_p	σ_{ft} (MPa)	σ_{fc} (MPa)	G_{IC} (J/m^2)
	3.73	0.38	0.3	61.6	300	334.1
Interphase	E_i (GPa)			σ_i (MPa)		
	22.5			670		
Interface	K (MPa/mm)	τ_1 (MPa)	τ_2, τ_3 (MPa)	G_{IC} (J/m^2)	G_{IIC}, G_{IIIC} (J/m^2)	
	10^8	70	80	2	32	

3. Failure envelopes obtained from computational micromechanics model

3.1. Failure envelopes of σ_{22}-τ_{12} and σ_{22}-τ_{23}

In this section, we utilize the computational micromechanics RVE model to predict the failure envelopes under multi-axial loading conditions, i.e. the failure loci for the whole range of combined stress states. First, the focus is put on the prediction of failure envelopes in the σ_{22}-τ_{12} and σ_{22}-τ_{23} stress planes. We adopt an RVE model with a thickness of $2R$, where R is the fiber radius. The influence of the loading path on the failure surfaces of UD CFRP composites subjected to transverse load and shear is analyzed through computational RVE model, as shown in Fig. 2(c) and (d). In the first loading path, the RVE was applied with a transverse load up to a prescribed stress level and then was deformed in shear until failure while the total transverse force acting on the RVE was held constant, which can be designated as $\sigma \rightarrow \gamma$ loading path. In the second path, the RVE is loaded simultaneously by proportional amounts of transverse and shear displacement, which can be designated as radial loading path.

The failure envelopes show that the loading path has a negligible influence on the failure envelopes, and the maximum shear strength increases by applying transverse compressive stress up to a transition point, before which it indicates a hardening effect of shear strength under moderate transverse compression. In this regime, the failure is shear dominated. With further increasing the magnitude of the transverse compression,

failure of the matrix under compression loading starts to dominate the failure process of composites, and the shear strength starts to decrease. In the transverse tension side, we observe that the shear strength decreases with the magnitude of transverse tension monotonically. Fig. 2(c) and (d) show the entire failure envelopes of σ_{22}-τ_{12} and σ_{22}-τ_{23} and the corresponding three dominant failure mechanisms or modes.

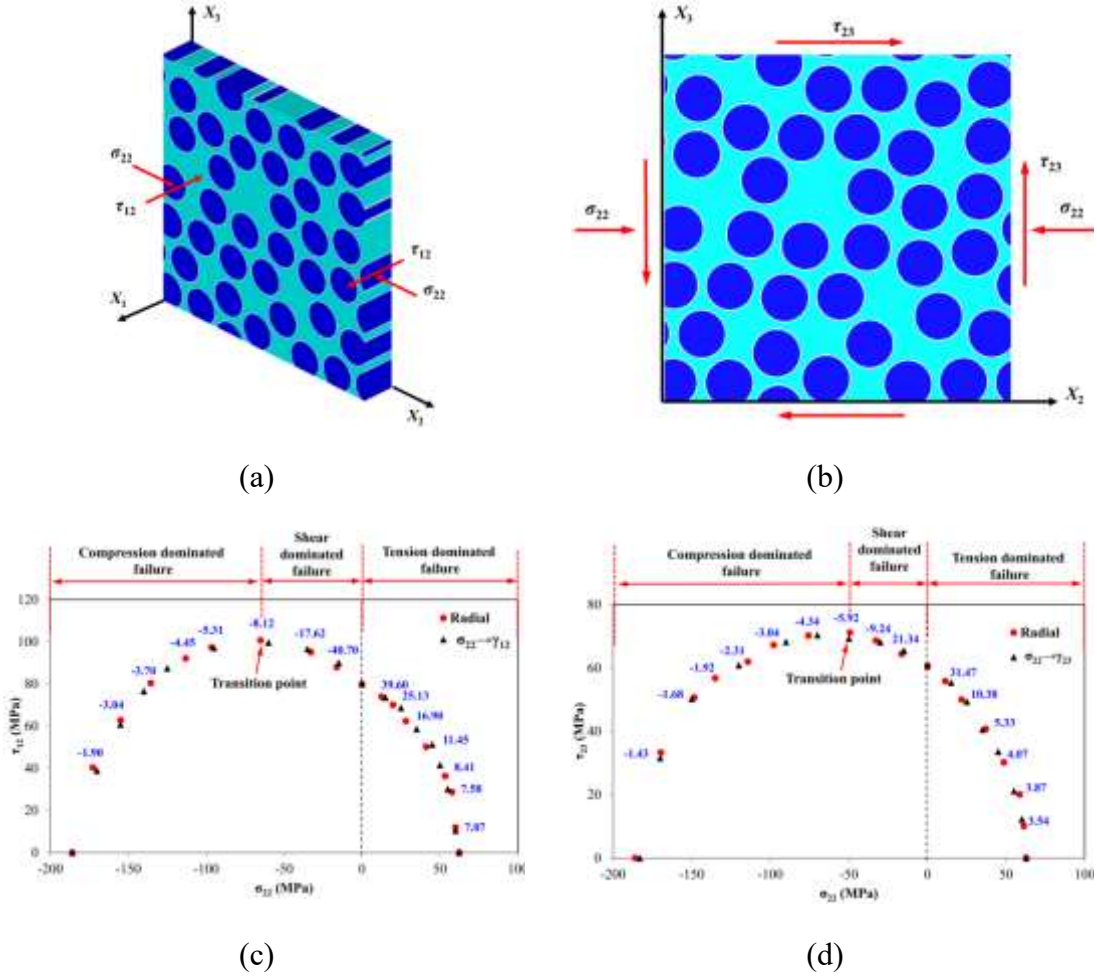

Figure 2. Schematic of the RVE of the UD CFRP composites subjected to (a) transverse load (σ_{22}) and in-plane shear (τ_{12}), (b) transverse load (σ_{22}) and out-of-plane shear (τ_{23}). (c) and (d) show the predicted failure envelopes of combined loading conditions corresponding to (a) and (b). The numbers next to the red points represent the ratio of shear displacement (δ_s) to transverse displacement ($\delta_{t/c}$ for either tension or compression).

This lack of sensitivity of the failure locus to the loading path is due to the fact that the initial failure is always interfacial debonding under combined uniaxial transverse tension and compression and combined in-plane and out-of-plane shear. The interfacial debonding tend to start at closely neighboring fibers where the stress

concentrations at the interfaces are higher, and interfacial debonding is corresponding to the peak point of the stress-strain curves obtained from the RVE model. Failure is also controlled by the same mechanisms under a combination of both stresses. The contour plots of the accumulated plastic strain after interface debonding for different ratios of $\delta_s/\delta_{t/c}$ are shown in Fig. 3. We can clearly observe that plastic deformation of the matrix and interphase region is only found around the interface cracks. The main matrix region of RVE model is still in the elastic state prior to fracture. Thus, failure envelopes depend primarily on the critical magnitude of the stresses that trigger interface debonding rather than on the loading path to reach the critical condition. Meanwhile, previous experimental results of AS4/PEEK composite subjected to longitudinal [27] or transverse compression [53] and numerical simulations of transverse compression combined with out-of-plane shear [54] or in-plane shear [53] did not detect any significant effect of the loading path on the failure locus either.

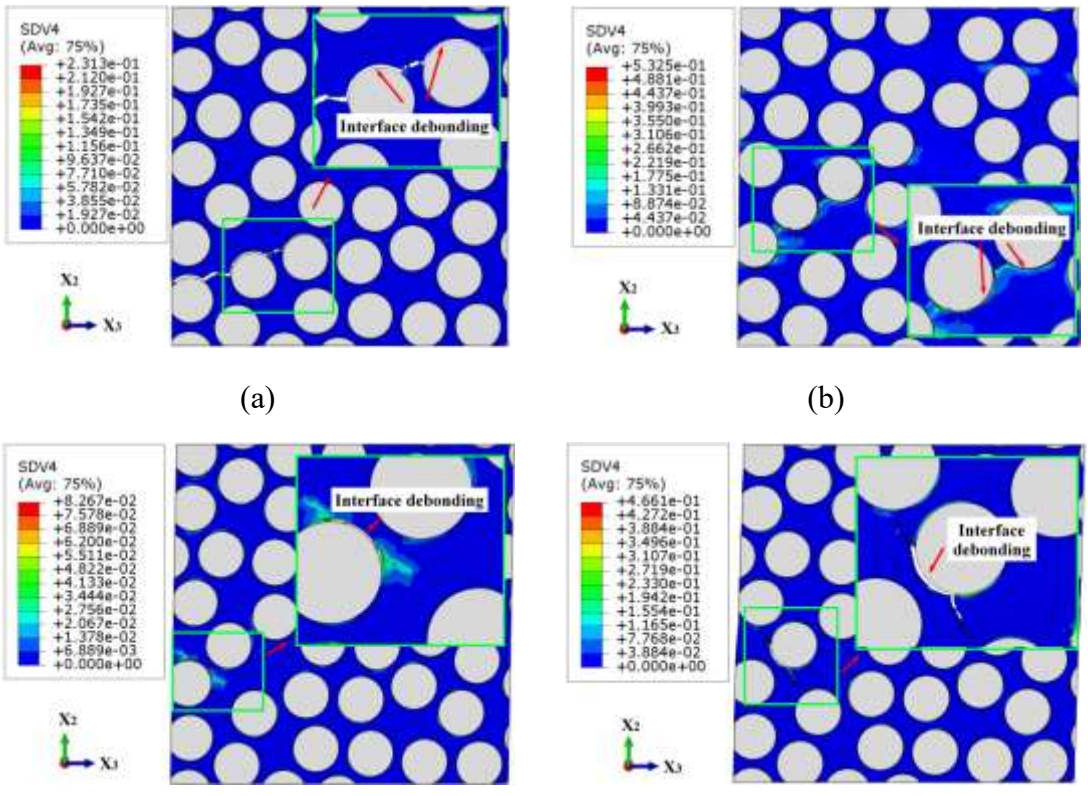

Figure 3. Contour plot of the accumulated plastic strain in the composites subjected to: (a) The ratio δ_s/δ_t of the radial loading path is 7.58 in the σ_{22}-τ_{12} stress space; (b) The ratio δ_s/δ_c of the radial loading path is -4.45 in the σ_{22}-τ_{12} stress space; (c) The

ratio δ_s/δ_t of the radial loading path is 5.33 in the σ_{22}-τ_{23} stress space; (d) The ratio δ_s/δ_c of the radial loading path is -2.31 in the σ_{22}-τ_{23} stress space. The plastic strain corresponding to each color is shown in the legend.

The detailed failure modes of the UD CFRP composites subjected to different loading conditions in the σ_{22}-τ_{12} stress space are presented in Fig. 4(a)-(f). For transverse tension side ($\sigma_{22}>0$), a fracture plane throughout the thickness direction is always generated. This fracture plane is formed by the normal interface debonding when the in-plane shear load is low, as shown in Fig. 4(a) and (b). While, with increasing the shear load, the complete fracture surface tends to tilt to an angle of 45° relative to the fiber direction (see Fig. 4(c)), which is similar to the pure in-plane shear loading case [30]. For the transverse compression side ($\sigma_{22}\leqslant 0$), the fracture plane is oblique, which causes the interfaces to be under tangential debonding other than normal opening. However, the in-plane shear loads induce a change in the fracture plane orientations. For instance, in the range of high shear loads ($-40.7 \leq \delta_s/\delta_c < -8.12$), the composite fails in shear-dominated mode and the final fracture angle is the same as the pure in-plane shear loading case, similar to Fig. 4(c). When the compressive stresses become more dominant as $-8.12 \leq \delta_s/\delta_c < 0$, the fracture occurs through a matrix plane whose inclination with respect to the X_2-direction increases gradually, as marked by the increasing angles show in Fig. 4 (d) - (f). When the compressive stress becomes large enough, the angle of the fracture surface with respect to X_2-direction saturates at around 57.8°, which is similar to the pure transverse compression loading case [30].

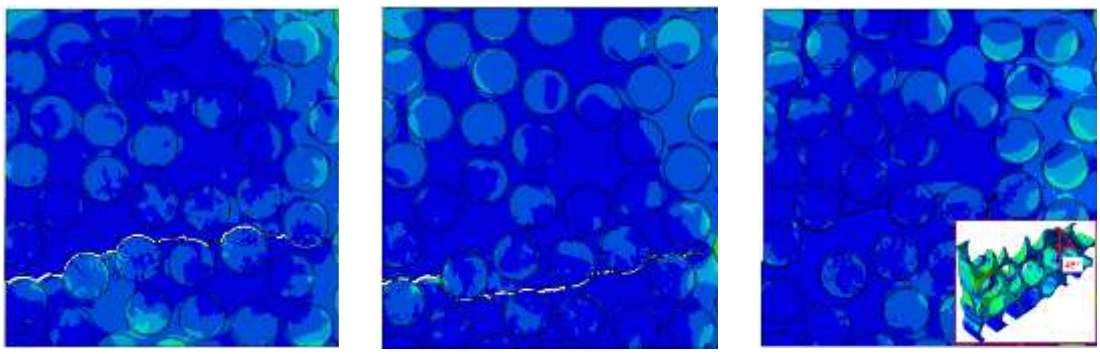

(a) (b) (c)

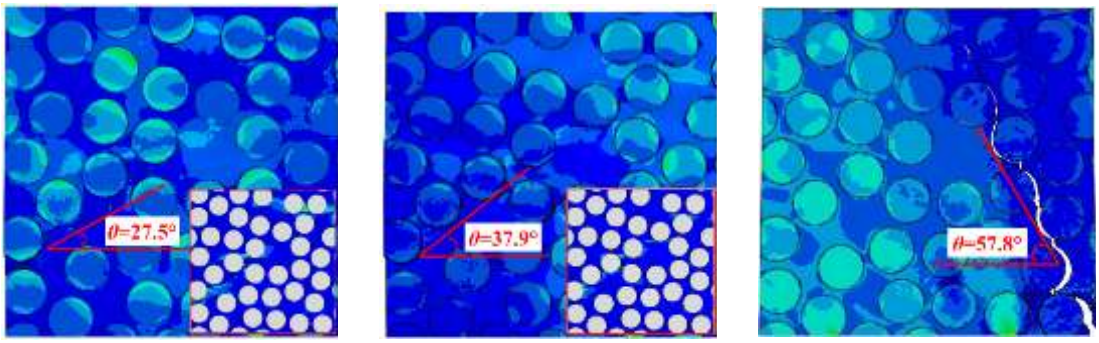

(d) (e) (f)

Figure 4. The failure modes of the UD CFRP composites under combined loading in the σ_{22}-τ_{12} stress space characterized by the ratio $\delta_s/\delta_{t/c}$. (a) $\delta_s/\delta_t = 7.58$, ($\varepsilon_{22} = 0.76\%$, $\gamma_{12} = 5.78\%$), (b) $\delta_s/\delta_t = 11.45$, ($\varepsilon_{22} = 0.51\%$, $\gamma_{12} = 5.78\%$), (c) $\delta_s/\delta_t = 25.13$, ($\varepsilon_{22} = 0.23\%$, $\gamma_{12} = 5.78\%$), (d) $\delta_s/\delta_c = -8.12$, ($\varepsilon_{22} = -0.71\%$, $\gamma_{12} = 5.78\%$), (e) $\delta_s/\delta_c = -4.45$, ($\varepsilon_{22} = -1.30\%$, $\gamma_{12} = 5.78\%$), (f) $\delta_s/\delta_c = -1.90$, ($\varepsilon_{22} = -3.04\%$, $\gamma_{12} = 5.78\%$).

The failure modes under combined transverse load and out-of-plane shear (σ_{22}-τ_{23} stress space) are presented in Fig. 5(a)-(f). It can be found that failure is always initiated by the nucleation of interface cracks depending on the contribution of transverse load and out-of-plane shear stresses. The stress concentration at the interface crack tip promotes the plastic deformation of the matrix, and then, damage localizes along the weakest path. Final failure occurs by the coalesce of interfacial cracks through the matrix. The orientation of the final fracture path varies as a function of the ratio of the applied transverse load and out-of-plane shear load. When it is shear dominant, the fracture plane is more towards an angle of 45° corresponding to X_2-direction, while if the transverse tension or compression dominates, the fracture plane is more towards 0° or 57.4°, respectively. For instance, in the transverse compression dominant case of $\delta_s/\delta_c = -1.43$ as shown in Fig. 5(f), the fracture plane is inclined at 57.4° to X_2-direction, showing good agreement with experimental observations of UD CFRP composites under solely transverse compressive loading [30].

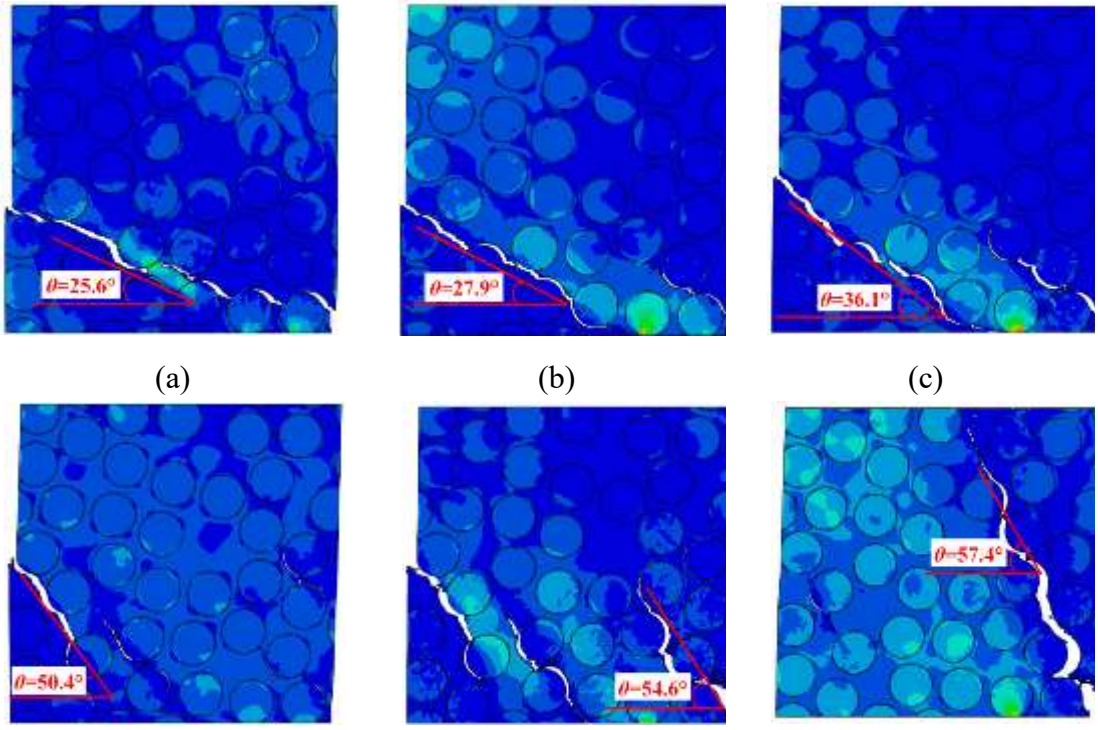

Figure 5. The failure modes of the UD CFRP composites under combined loading in the σ_{22}-τ_{23} stress space for different ratios of $\delta_s/\delta_{t/c}$. (a) $\delta_s/\delta_t = 3.87$, ($\varepsilon_{22} = 0.78\%$, $\gamma_{23} = 3.03\%$), (b) $\delta_s/\delta_t = 5.33$, ($\varepsilon_{22} = 0.57\%$, $\gamma_{23} = 3.03\%$), (c) $\delta_s/\delta_t = 10.38$, ($\varepsilon_{22} = 0.30\%$, $\gamma_{23} = 3.03\%$), (d) $\delta_s/\delta_c = -5.92$, ($\varepsilon_{22} = -0.51\%$, $\gamma_{23} = 3.03\%$), (e) $\delta_s/\delta_c = -2.3$, ($\varepsilon_{22} = -1.31\%$, $\gamma_{23} = 3.03\%$), (f) $\delta_s/\delta_c = -1.43$, ($\varepsilon_{22} = -2.12\%$, $\gamma_{23} = 3.03\%$).

3.2. Failure envelope of σ_{11}-τ_{12}

Kink-bands typically initiate in the regions of fiber waviness/misalignment [33] or where fiber rotations have been introduced by other failure mechanisms (e.g. delamination of neighboring plies [55], following a shear-driven fiber compressive failure [56]). Under compressive load, initially misaligned fibers rotate and lead to shear stresses in the matrix. As the matrix fails, the fibers lose the support which results in further fiber rotation and deformation of the kink-band [33]. Recently, Bai et al. [57] presented a 3D RVE investigation of the formation of kink-band under longitudinal compression of the composites. In this section, we further extend that work in the fiber longitudinal direction by considering local fiber waviness, which is characterized in an interval between $x_1 \leqslant x \leqslant x_2$ in the longitudinal direction located at the middle of the 3D RVE model, as shown in Fig. 6(a). The total length of the 3D

RVE model is $L_T = 700\ um$. We use half of the wavelength of a cosine wave to represent the fiber waviness, and the wavelength (L=1000 um) is estimated by evaluating the experimental sample [33], which is assumed to be constant for all the fibers in the computational micromechanics RVE model. Different maximum waviness angles (θ_{max}) can be achieved by changing the wave amplitudes (A). Fig. 6(a) shows the imperfection area and the parameters for the local fiber waviness.

The waviness function of the bottom boundary is given by:

$$\mathrm{y} = \begin{cases} 0 & 0 \le x < x_1 \\ A\cos(2\pi x/L) & x_1 \le \mathrm{x} \le x_2 \\ A & x_2 < \mathrm{x} \le L_T \end{cases} \quad (1)$$

The initial misalignment is geometrically introduced according to the derivation of y(x),

$$tan\theta(x) = -\frac{2\pi \mathrm{A}}{L}\sin(2\pi x/L) \quad (2)$$

Imperfections stemming from the manufacturing process influence the compressive strength and fiber kinking of unidirectional composites significantly. In fact, previous studies have acknowledged that the compressive strength of fiber composites is highly dependent on initial fiber misalignment [33, 58-60]. It is, however, difficult to determine the initial fiber misalignment angle since manufacturing defects appear stochastically. In this section, a parametric study relating to θ_{max} is first conducted using our computational model. The compressive strength is found to decrease with increasing θ_{max}, as shown in Fig. 6(b). Thus, θ_{max} can be used as a representative parameter to describe the scale of fiber waviness from different manufacturing conditions.

A large variety of analytical models to predict the strength related to fiber kinking under pure longitudinal compressive loading can be found in the literature [11, 61]. Recently, Pinho and coworkers [62] have proposed a theoretical model to predict the compressive strength depending on the initial fiber waviness angle under pure longitudinal compressive loading:

$$X_c = \frac{V^f}{(1 - V^f)/G_m + \theta_{max}/S_L^{is}} \tag{3}$$

where V^f is fiber volume fraction, G_m is matrix shear modulus, $\theta_{\max}$ is the maximum fiber waviness angle and s_L^{is} is the in-situ in-plane shear strength of the composite.

Fig. 6(b) also shows the comparison of longitudinal compressive strength obtained computationally and theoretically using Eq. (3). We can find that the computational and analytical results show excellent agreement. We would like to point out that for θ_{max}=5.4°, the compressive strength decreases by approximately 70%. It indicates that the compressive strength is very sensitive to the initial fiber waviness introduced during manufacturing processes.

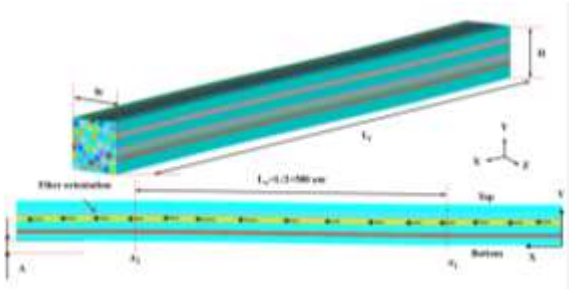

(a)

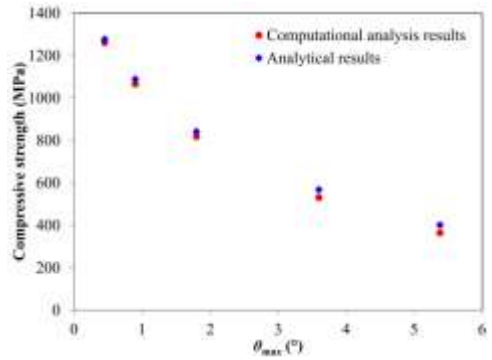

(b)

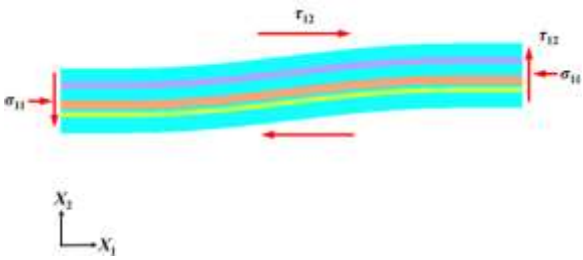

(c)

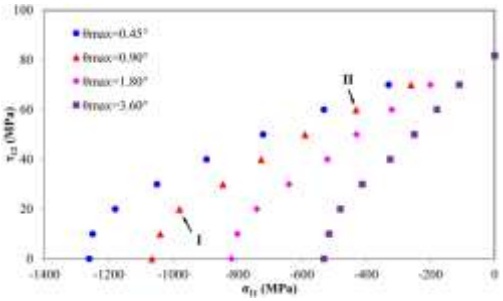

(d)

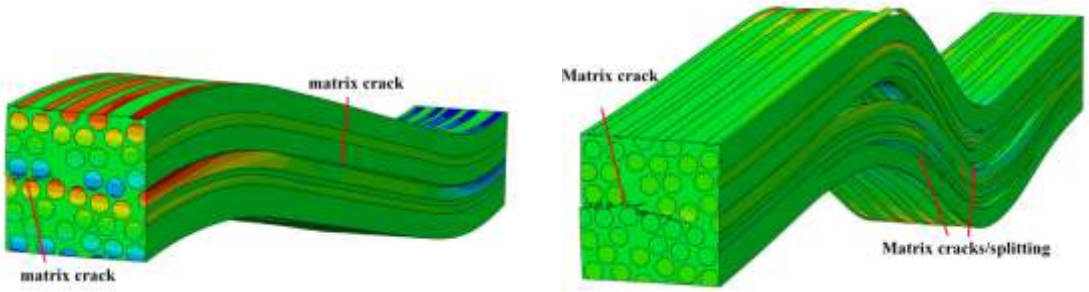

(e) (f)

Figure 6. (a) Schematic of the computational model considering local fiber waviness (L_W=L/2=500 *um*, L_T=700 *um*). (b) Comparison between the predicted longitudinal compressive strength values from RVE models and analytical solutions proposed by Pinho et al. [62]. (c) Schematic of computational micromechanics model subjected to the stress state of σ_{11}-τ_{12}. (d) Failure envelopes of σ_{11}-τ_{12} for different θ_{max}. (e) and (f) show the failure modes which correspond to the points I and II in panel (d) for θ_{max}=0.90°, respectively.

The experimental determination of the failure envelope of σ_{11}-τ_{12} is very difficult to set up. To overcome these difficulties and determine the failure envelope of σ_{11}-τ_{12}, in-plane shear load (τ_{12}) is applied simultaneously with longitudinal compression (σ_{11}) using our computational micromechanics model, as shown in Fig. 6(c). Shear forces are applied at x_1 = 0 and L_T. A compressive displacement is applied at $x_1 = L_T$, while the displacements in the x_1- direction are restricted at x_1=0.

Taking advantage of the RVE model, we further investigate the effect of fiber misalignment, i.e. maximum waviness angle θ_{max} on the shape and magnitude of the failure envelope in the space of σ_{11}-τ_{12}. From Fig. 6 (d), we can see that the σ_{11}-τ_{12} envelopes rotate around the point (σ_{11}=0, τ_{12}=S_L) and increasing θ_{max} leads to a significant decrease of the domain defined by the area under the failure envelopes. In addition, the longitudinal compressive strength decreases with increasing τ_{12}. Interestingly, we find that the in-plane shear load changes the kink-band failure mechanism of UD CFRP composites, and we observe that the main failure mode changes from fiber kink to matrix cracking/splitting with increasing τ_{12}. Meanwhile, the area of matrix cracking goes up with increasing τ_{12}, as shown in the comparison between Fig. 6(e) and (f).

4. Comparison between the classical failure criteria and numerical results

4.1. A brief overview of the classical failure criteria

Currently, there exist numerous failure criteria which are usually stress-based and expressed as equations, including fully interactive criteria (Tsai Wu [63], Tsai Hill [64]) and failure mode based criteria (Hashin [65], Puck [10], and Pinho-LaRC04 [11, 12]. In a recent study, Daniel-NU failure theory [17, 66], which is based on micromechanical matrix failure mechanisms, allows the prediction of failure envelopes under multi-axial stress states at different strain rates. The strain-rate effect is considered by developing an equation of the matrix strength as a function of the strain rates.

Tsai Wu [63] and Tsai Hill [64] criteria predict failure load by using equations involving all stress components, which combine different fundamental fracture mechanisms together. Different from Tsai Wu and Tsai Hill criteria, in the work by Hashin and Rotem [65], the failure of laminated composites has been categorized into fiber-dominated failure and matrix-dominated failure, and either one is further subdivided into tensile and compressive modes. In addition, they assume that failure is induced by the normal and tangential stresses acting on the fracture plane. One disadvantage of Hashin's criterion is that it neglects the shear hardening effect with the presence of transverse compression [12]. Hashin's approach has been further extended by Puck and Schuermann [10] by addressing matrix compression failure with a model based on the Mohr-Coulomb criterion, where Puck distinguishes different fracture modes according to the stress combinations which appear on the detected fracture plane. Afterwards, Pinho and coworkers [11, 12] adopted a similar assumption and implemented the action plane concept according to the Mohr-Coulomb criterion. Concerning tensile matrix cracking, LaRC03 [13] is associated with Dvorak's fracture mechanics approach [67], using the energy release rates associated with intralaminar crack propagation. Subsequently, the LaRC04 criterion was developed by extending the approach to three-dimensional stress states and taking into account the non-linear matrix shear behavior [12].

4.2. Assessments of classical failure criteria by comparison with numerical failure envelopes

Following the recent collaborative work carried out in WWFE, a number of failure criteria have been compared to corresponding experimental characterizations. However, the physical failure mechanisms and the mechanical strengths are notoriously difficult to be validated experimentally for multi-axial stress states, and the capability of these criteria in predicting ultimate strength of composite composites under multi-axial loading remains unclear. The computational model presented here provides a great advantage to evaluate the performance of ply-level composites failure criteria for complex stress states by replacing experimental tests.

The failure envelopes under transverse load and in-plane/out-of-plane shear (σ_{22}-τ_{12} and σ_{22}-τ_{23}) from our computational results are compared with those predicted by the classical failure criteria, as shown in Fig. 7(a) and (b). The results show that there exist large variances among different criteria.

We first compare our computational results and these failure criteria in the range of $\sigma_{22}>0$. In the stress space of σ_{22}-τ_{12}, the predictions by Tsai-Wu [63], Daniel [17, 66] and Puck [10] are almost identical with the computational results, while Hashin's [9, 65] and Pinho's [11, 12] slightly overestimate the failure strengths of τ_{12} in the stress plane of σ_{22}-τ_{12}. In terms of the stress space of σ_{22}-τ_{23}, Hashin's predictions are almost consistent with the computational results in the range of $\sigma_{22}>0$, while Pinho's slightly overestimate, Tsai-Wu's and Puck's values slightly underestimate failure strengths of τ_{23} for a high ratio of δ_s/δ_c. It should be noted that the accuracy of predictions of τ_{23} depends upon the suitable determination of S^T, which is very difficult to measure experimentally.

In the range of $\sigma_{22}\leqslant 0$, the curves predicted by these failure criteria show greater differences from each other, especially with the presence of high shear stress in both σ_{22}-τ_{12} and σ_{22}-τ_{23}. The envelopes predicted by Hashin's 1980 criterion [9] provides a modest improvement in accuracy compared to the 1973 version [65], but still underestimate failure strength compared with computational results. Pinho's and

Daniel's criteria capture the shear strength increase at the initial stage of compressive σ_{22}, but their predicted values are slightly higher than the results from our computational micromechanics model. In the σ_{22}-τ_{12} stress space, Puck's criterion agrees with computational results in low σ_{22} regime but overestimates the strengths in the high σ_{22} regime. In σ_{22}-τ_{23} stress space, Puck's and Daniel's criteria perform better with only slight overestimations in the medium σ_{22} regime. Among all these criteria, we can find that Tsai Wu's criterion agrees with the computational results the best, as the predicted failure envelope of σ_{22}-τ_{23} is nearly identical to the computational one.

For the stress states that involve longitudinal compression (σ_{11}-τ_{12}), the same disparity is found when different failure criteria are compared with our computational results. Fig. 7(c) shows the failure envelopes σ_{11}-τ_{12} generated by the computational micromechanics model and the corresponding classical failure criteria. For Hashin's [65] and Puck's criteria [10], the compressive strength is not affected by the shear stress. Their failure envelopes show a rectangular or approximately rectangular shape. In contrast, Edge's [68] and Pinho's predicted a linear failure envelope based on the assumption that the buckling of the fibers under compression is promoted by the presence of in-plane shear stress. The failure criteria of Tsai-Wu and Tsai-Hill are a polynomial based criterion and their failure surfaces have an ellipsoid shape. Our computational results fall between the linear and ellipsoid envelopes.

Comparing the results from our computational analysis and these classical failure criteria, although most of these failure criteria provide a similar trend for the loading conditions of σ_{22}-τ_{12} and σ_{22}-τ_{23}, there exists some difference for combined loading conditions for $\sigma_{22} \leqslant 0$ in σ_{22}-τ_{12} and σ_{22}-τ_{23} stress space, especially with the presence of high shear stress. One possible reason is that most of the classical failure criteria did not consider the transitions of failure mechanisms observed in section 3.1. Furthermore, most of the current failure criteria are not accurate enough to describe our computational results of σ_{11}-τ_{12}. So, the current failure criteria are not completely applicable to the CFRP composites studied here. It is thus important to develop a new set of comprehensive and effective failure criteria to better predict the failure

envelopes of the CFRP composites.

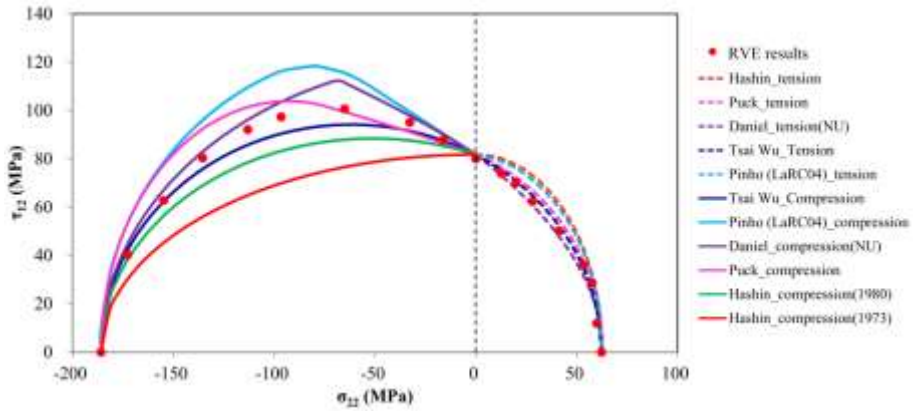

(a)

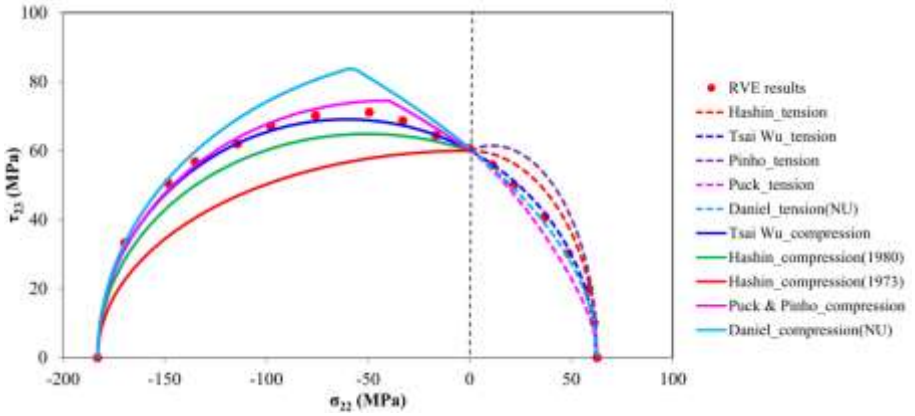

(b)

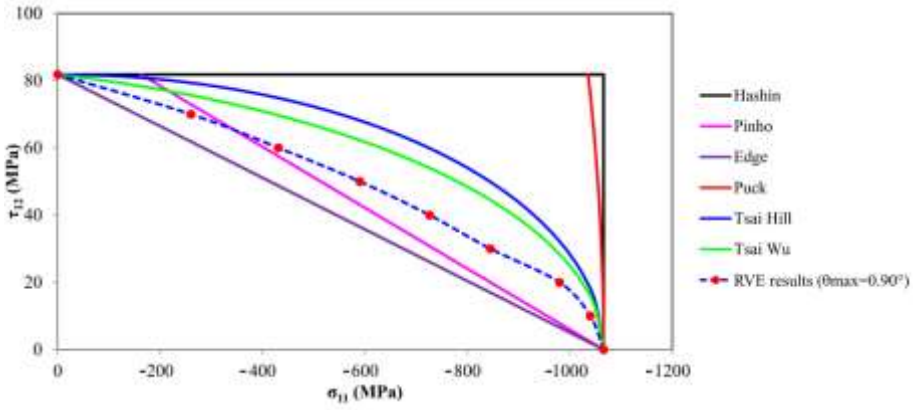

(c)

Figure 7. Failure envelopes of (a) σ_{22}-τ_{12} and (b) σ_{22}-τ_{23} for the radial loading path, showing the difference between Hashin, Tsai-Wu, Pinho, Daniel, Puck failure criteria and computational results. (c) Comparison of the failure envelopes of σ_{11}-τ_{12} obtained from the computational micromechanics model using θ_{max}=0.90° and different failure criteria.

5. Proposed failure criteria and the validation

5.1. Proposed failure criteria

A new set of homogenized failure criteria of σ_{22}-τ_{12} and σ_{22}-τ_{23} is proposed here based on the computational micromechanics RVE analysis. We have identified three dominant failure mechanisms or modes from the computational RVE model under multi-axial loading conditions, which is tension, shear, and compression dominated failure modes. These three dominant failure mechanisms resemble those proposed by the NU-Daniel failure criteria. So, we propose a new set of failure criterial based on the NU-Daniel failure criteria as shown in Table 2. A key element in the proposed failure criteria for σ_{22}-τ_{12} and σ_{22}-τ_{23} is the determination of the stress value of the transition point, as shown in Fig. 8(a) and (b). The transition point is a critical point for the transition from shear dominated failure to compression dominated failure. The value can be obtained from computational analysis or experimental testing under combined loading conditions.

Table 2. Comparison of the NU-Daniel failure criteria and the proposed failure criteria for the σ_{22}-τ_{12} stress space

	NU-Daniel	Proposed failure criteria	
Tension dominated failure ($\sigma_{22} > 0$)	$\frac{\sigma_{22}}{Y^T} + \left(\frac{a}{2}\right)^2 \left(\frac{\tau_{12}}{Y^T}\right)^2 = 1$	$\frac{\sigma_{22}}{Y^T} + \left(\frac{\tau_{12}}{S^L}\right)^2 = 1$	(4)
Shear dominated failure ($\sigma_{22}^{Tran} < \sigma_{22} \leq 0$)	$\left(\frac{\tau_{12}}{S^L}\right)^2 + \frac{2}{\alpha}\frac{\sigma_{22}}{S^L} = 1$	$\left(\frac{\tau_{12}}{S^L}\right)^2 + \alpha\frac{\sigma_{22}}{Y^T} = 1$ $\alpha = \frac{Y^T}{\lvert\sigma_{22}^{Tran}\rvert}\left[\left(\frac{\lvert\tau_{12}^{Tran}\rvert}{S^L}\right)^2 - 1\right]$	(5)
Compression dominated failure ($-Y^C \leq \sigma_{22} \leq \sigma_{22}^{Tran}$)	$\left(\frac{\sigma_{22}}{Y^C}\right)^2 + \alpha^2\left(\frac{\tau_{12}}{Y^C}\right)^2 = 1$ $\alpha = 2\frac{Y^T}{S^L}$	$\left(\frac{\sigma_{22}}{Y^C}\right)^2 + \beta^2\left(\frac{\tau_{12}}{Y^C}\right)^2 = 1$ $\beta = \frac{Y^C - \lvert\sigma_{22}^{Tran}\rvert}{S^L}$	(6)

In Table 2, σ_{22} and τ_{12} are transverse normal stress and in-plane shear stress; σ_{22}^{Tran} and τ_{12}^{Tran} are transverse normal and in-plane shear stress of the

transition point; Y^T, Y^C, and S^L are the transverse normal tensile and compressive strengths and in-plane/out-of-plane shear strength, respectively; α and β are the material parameters. By changing τ_{12} and S^L to τ_{23} and S^T in the Eqs. (4)-(6), we can obtain the failure criteria for a combined load of σ_{22}-τ_{23}, where S^T is the out-of-plane shear strength.

Based on Puck's theory [10, 69], the values of transition points, i.e., σ_{22}^{Tran}, τ_{12}^{Tran} and τ_{23}^{Tran}, can also be predicted by the following equations if there are no computational or experimental results available:

$$|\sigma_{22}^{Tran}| = \frac{Y^C}{2\left(1+p_{\perp\perp}^{(-)}\right)} \tag{7}$$

$$|\tau_{12}^{Tran}| = S^L\sqrt{1+2p_{\perp\perp}^{(-)}},\ |\tau_{23}^{Tran}| = S^T\sqrt{1+2p_{\perp\perp}^{(-)}} \tag{8}$$

$$p_{\perp\perp}^{(-)} = \frac{1}{2}\left[\sqrt{1+2p_{\perp||}^{(-)}\frac{Y^C}{S^{L/T}}}-1\right] \tag{9}$$

where the recommended range of $p_{\perp||}^{(-)}$is 0.20 to 0.25 for glass-fiber reinforced composites and 0.25 to 0.30 for carbon-fiber reinforced composites [69]. Once the values of $p_{\perp||}^{(-)}$is determined, $p_{\perp\perp}^{(-)}$ can be calculated according to Eq. (9).

For the loading cases that involve longitudinal compression failure ($\sigma_{11} \leq 0$), the main dominant failure mechanisms identified from the computational micromechanics model changes from fiber kink to matrix cracking/splitting with increasing in-plane shear load. Since Tsai-Wu's prediction agrees with our computational results the best, we modify Tsai-Wu's failure criterion of σ_{22}-τ_{12} by also considering the dependence of compressive strength on the initial fiber waviness angle (Eq.3). The comparison between them are listed in Table 3. We note that X^C and X^T is longitudinal compressive and tensile strength, respectively.

Table 3. Comparison of the proposed failure criteria and the Tsai-Wu's failure criterion for the σ_{11}-τ_{12} stress spac

	Tsai-Wu	Proposed failure criteria	
Fiber-compression dominated failure ($\sigma_{11} \le 0$)	$F_{11}\sigma_{11}^2 + F_1\sigma_{11} + \left(\frac{\tau_{12}}{S^L}\right)^2 = 1$ $F_{11} = \frac{1}{X^T X^C}, F_1 = \left(\frac{1}{X^T} - \frac{1}{X^C}\right)$	$-\frac{\sigma_{11}}{X^C} + \left(\frac{\tau_{12}}{S^L}\right)^2 = 1$ $X_c = \frac{V^f}{\frac{(1-V^f)}{G_m} + \frac{\theta_{max}}{S_L^{is}}}$	(10)

We compare the computational results and the proposed failure criteria for several stress states Fig. 8. The material properties used in the failure criteria are listed in Table 4. We can find that the new set of failure criteria are in very good agreement with computational RVE results. This demonstrates that by taking the advantage of computational results, either current failure criteria can be improved or better ones for the investigated composites can be proposed.

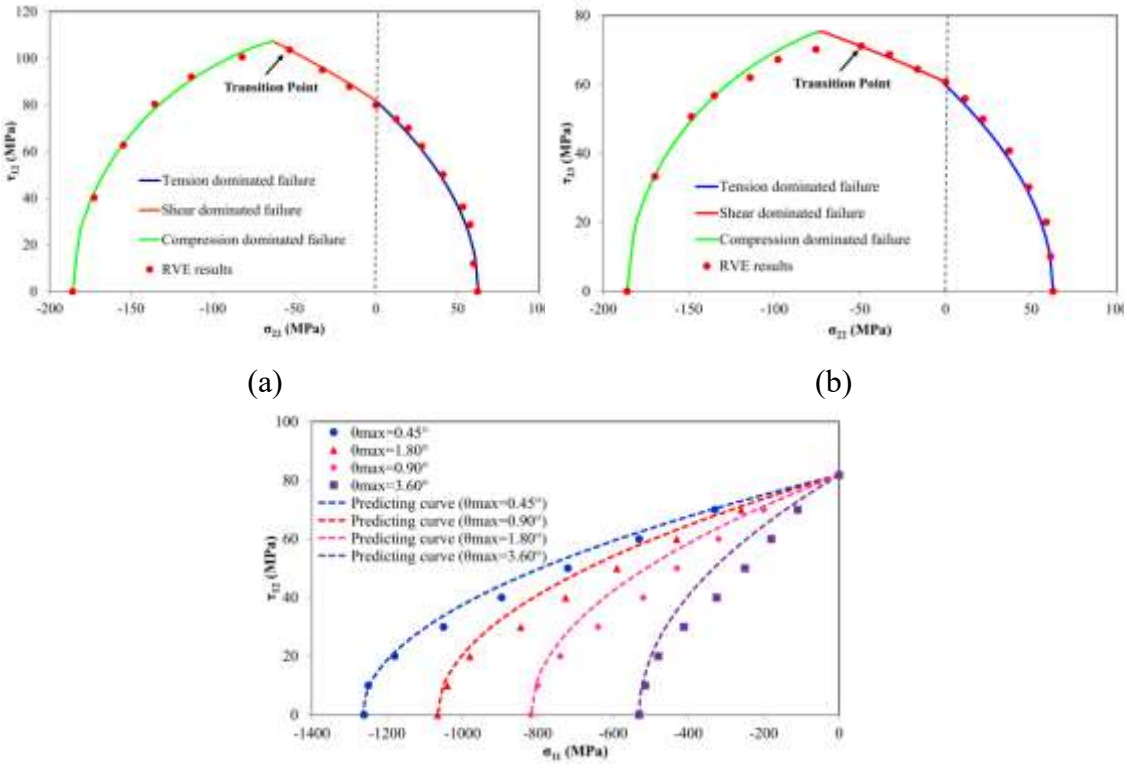

Figure 8. Comparison of the failure envelopes for the radial loading path obtained from the computational RVE model and the proposed failure criteria. (a) σ_{22}-τ_{12}, (b) σ_{22}-τ_{23}, and (c) σ_{11}-τ_{12}.

Table 4. Material properties of UD CFRP composites

Y^T	Y^C	S^L	S_L^{is}	S^T	$(\lvert\sigma_{22}^{Tran}\rvert, \lvert\tau_{12}^{Tran}\rvert)$	$(\lvert\sigma_{22}^{Tran}\rvert, \lvert\tau_{23}^{Tran}\rvert)$
(MPa)	(MPa)	(MPa)	(MPa)	(MPa)	(MPa, MPa)	(MPa, MPa)
62.75	185.9	81.8	113.3	60.7	(53, 103.7)	(49, 71)

5.2. Validation of the proposed failure criteria

5.2.1. Failure envelopes of σ_{22}-τ_{12}

To evaluate and validate the failure envelope of σ_{22}-τ_{12} obtained from proposed failure criteria, we also conduct off-axial tests to measure the failure strengths under multi-axial loading conditions [70, 71].

We choose five different off-axis angles (i.e. θ=10°, 30°, 45°, 60°, and 90°) of UD CFRP specimens for the experimental analysis. The geometries of these specimens are identical as shown in Fig. 9(a). According to the given off-axis angles, the off-axis specimens are cut from the laminated plates using a diamond saw and polished with standard techniques. To reduce the gripping effects, woven glass/epoxy tabs are used on the specimens. Compressive and tensile tests are conducted in accordance with ASTM Standards D6641 [52] and D3039 [53], respectively. AMTS Sintech test machine fitted with a 30000 *lb*. load cell is used to determine the transverse behavior of the UD CFRPs with a crosshead speed of 2 *mm*/*min*.

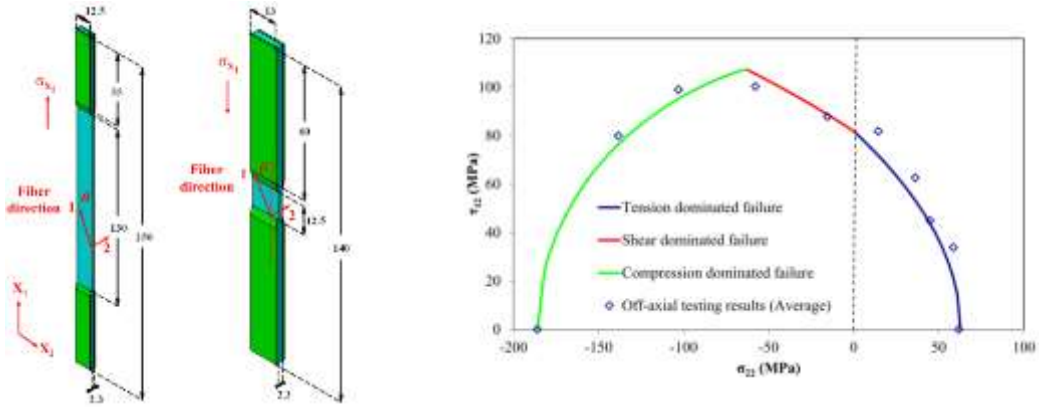

(a) (b)

Figure 9. (a) Geometries of off-axis specimen (unit: *mm*). (b) Comparisons between failure envelopes of σ_{22}-τ_{12} obtained from proposed failure criteria and our

experimental tests.

For the off-axis specimen, the stresses in a ply with fibers oriented at an angle θ to the direction of the applied stress can be obtained as follows:

$$\sigma_{11} = \sigma_{x_1} \cos^2 \theta \, , \sigma_{22} = \sigma_{x_1} \sin \theta \, , \tau_{12} = -\sigma_{x_1} \sin \theta \cos \theta \tag{11}$$

where σ_{11}, σ_{22} and τ_{12} are stresses in the material axis, σ_{x_1} is the off-axis loading stress. The corresponding σ_{11u}, σ_{22u} and τ_{12u} can be obtained by plugging the off-axis ultimate strength σ_{x_u} into Eq. (11).

The experimental results obtained are not scattered and thus this set of experimental data is ideal to check the applicability of the proposed failure criteria. Fig. 9(b) shows the comparisons between failure envelopes of σ_{22}-τ_{12} obtained from experimental results and analytical results. It is shown that the proposed failure criteria are in very good agreement with experimental results. Thus, the failure criteria proposed here are proved to be sufficient to describe the failure envelopes of UD CFRP composites in the σ_{22}-τ_{12} stress space.

To check whether the proposed failure criteria are generally applicable to other UD reinforced composites for the failure envelopes of σ_{22}-τ_{12}, a comparison is made with six sets of experimental data found in the literature [17, 18, 72-75]. The mechanical properties for these materials needed to generate the corresponding failure envelopes are reported in Table 5. Fig. 10 shows the comparisons between failure envelopes of σ_{22}-τ_{12} obtained from the proposed failure criteria and these experimental testing data. Good agreements between the predictions and experimental data are generally observed. As a result, the proposed failure criteria which considers the transitions of failure mechanisms can be also applied to different types of fiber reinforced composites.

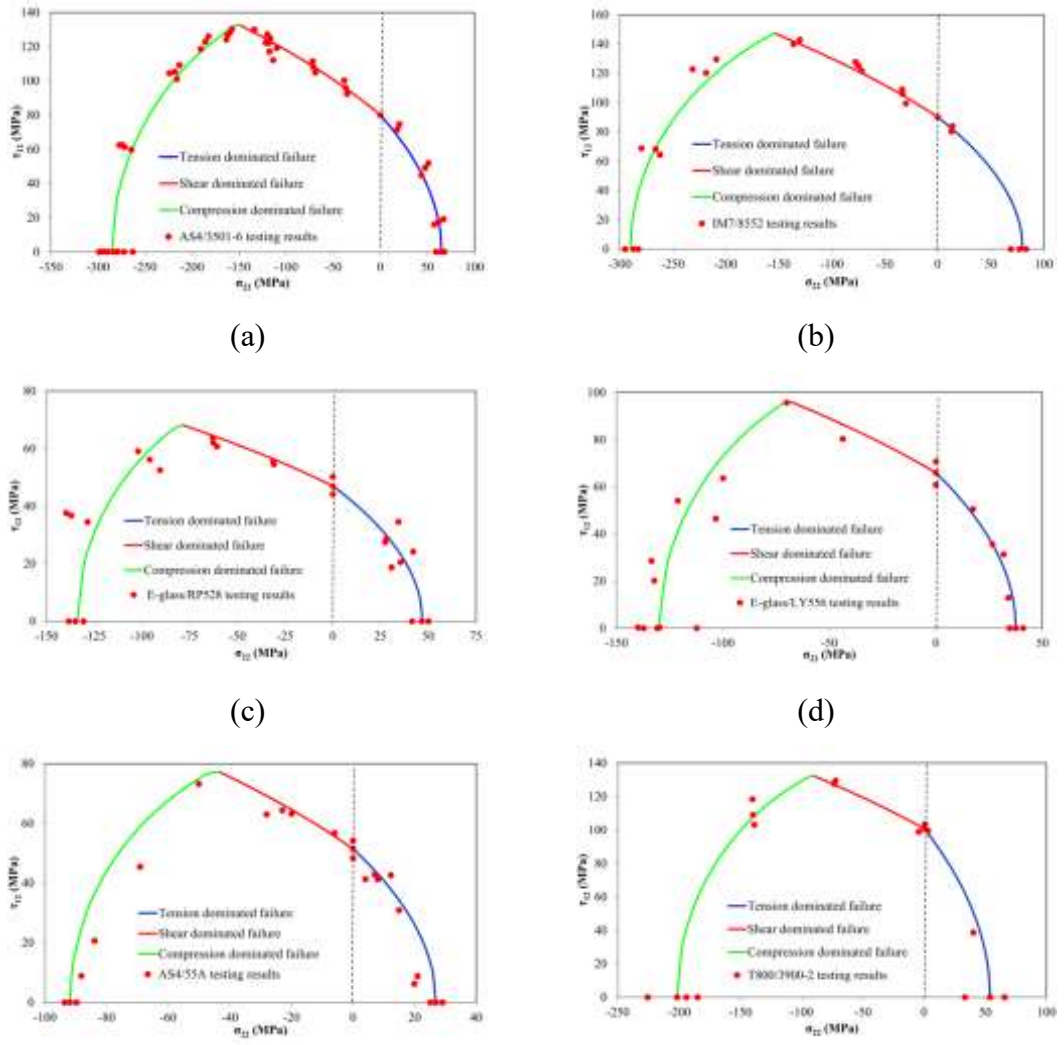

Figure 10. Comparison between failure envelopes of σ_{22}-τ_{12} predicted by the proposed failure criteria and experimental data on different materials: (a) AS4/3501-6 [72], (b) IM7/8552 [17], (c) E-glass/RP528 [73], (d) E-glass/LY556 [74], (e) AS4/55A [18], and (f) T800/3900-2 [75].

Table 5. Material properties of different composites

Material	AS4/ 3501-6	IM7/ 8552	E-glass/ RP528	E-glass/ LY556	AS4/ 55A	T800/ 3900-2
Ref.	[72]	[17]	[73]	[74]	[18]	[75]
X^T (MPa)	2300	2280	-	1140	-	-
X^C (MPa)	1725	1725	-	570	-	-
Y^T (MPa)	60.2	80	47	37.5	27	48.8
Y^C (MPa)	275.8	290	134	130.3	91.8	201.7
S^L (MPa)	73.4	90	47	66.5	51.3	53
$\lvert\sigma_{22}^{Tran}\rvert$ (MPa)	140	140	65	55	39	73
$\lvert\tau_{12}^{Tran}\rvert$ (MPa)	130	143	65	91	75	127

5.2.2. Failure envelopes of σ_{11}-τ_{12}

Experimental determination of the failure envelopes for the combined in-plane shear/longitudinal compression (σ_{11}-τ_{12}) is much more complex. Here, we refer to the limited experimental data found in the literature. Fig. 11 shows the failure envelopes generated by the proposed failure criteria and the corresponding experimental data determined by the torsion and compression tests of tubes [76-78]. The relevant mechanical properties of the material are shown in Table 6. The results show that the predictions of the proposed failure criteria are in good agreement with the experimental data of Soden et al. [78], as shown in Fig. 10(a) and (b). However, some discrepancies between the predicted results and the experimental data of Michaeli et al. [77] and Chandra et al. [76] are shown in Fig. 11(c) and (d). Large scatters also exist in these two sets of experimental data, which is possibly due to largely variant fiber misalignment or waviness in the specimens. Nevertheless, the general trend of failure strengths in the σ_{11}-τ_{12} stress space is captured by the proposed failure criteria.

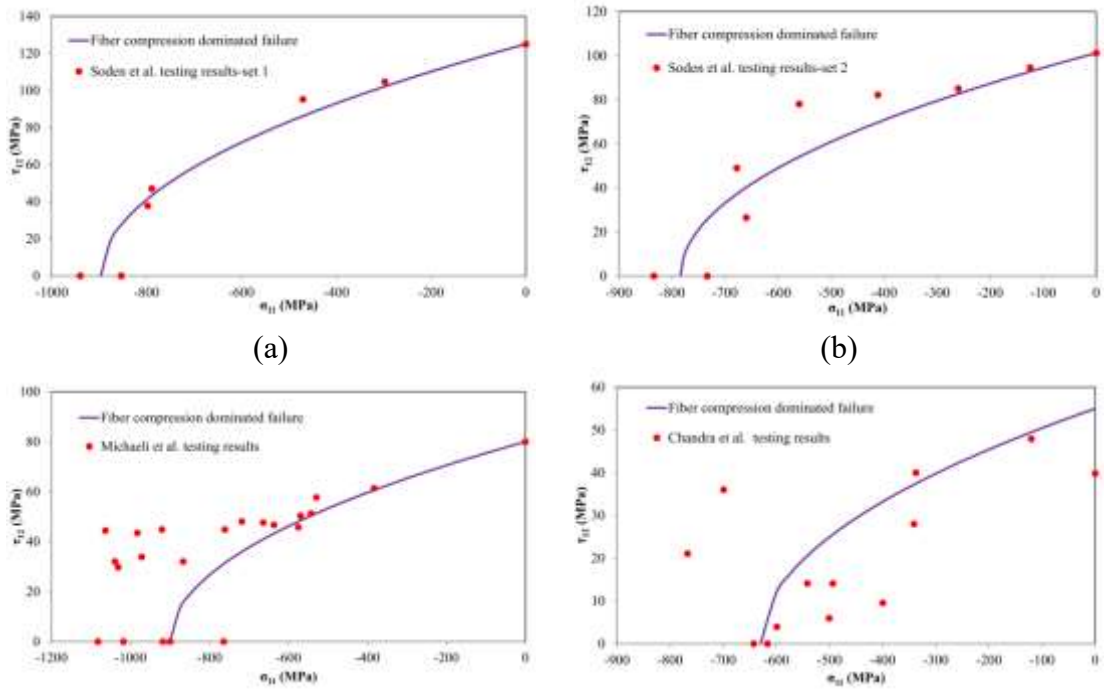

(a) (b)

(c) (d)

Figure 11. Comparison between failure envelopes of σ_{11}-τ_{12} predicted by the proposed failure criteria and experimental data on different materials: (a) and (b) T300/914C [78], (c) T300/LY556/HY917/DY070 [77], and (d) E-glass/411-C50 [76].

Table 6. Material properties of investigated composites

Material	T300/914C Set 1 [78]	T300/914C Set 2 [78]	T300/LY556/HY917 /DY070 [77]	E-glass/ 411-C50 [76]
X^C (MPa)	898.6	784	900	629.8
S^L (MPa)	125	101.25	80	55

5.2.3. Failure envelopes of σ_{22}-τ_{23}

The stress states of σ_{22}-τ_{23} are extremely difficult to realize experimentally because geometries of the test specimens are extremely difficult to obtain. However, computational analysis has been used to generate failure envelopes of σ_{22}-τ_{23}. So, we validate the proposed failure criteria with computational results found in the literature [18, 37]. Table 7 lists the material properties used in these computational models. Fig. 12(a) and (b) show the comparison between the failure envelopes of σ_{22}-τ_{23} found in two studies and the failure criteria proposed herein. Again, the transitions of failure mechanisms well describe the characteristics of these failure envelopes, which further justifies the applicability of the proposed failure criteria.

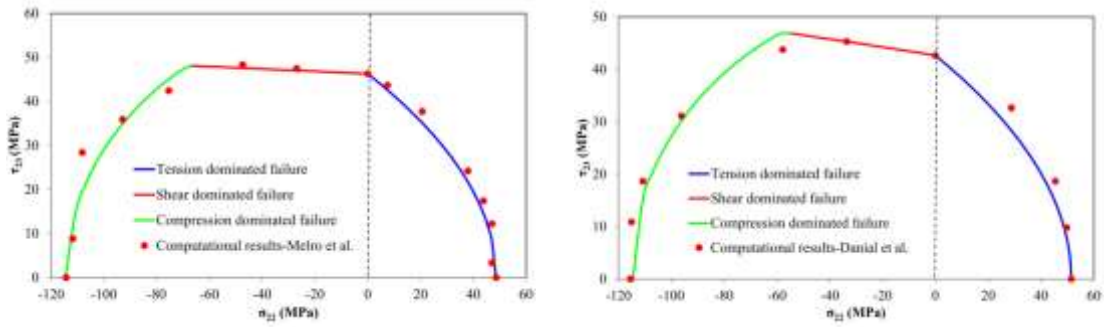

(a) (b)

Figure 12. Comparison between failure envelopes of σ_{22}-τ_{23} predicted by the proposed failure criteria and computational results from (a) Melro et al. [18], and (b) Danial et al. [37].

Table 7. Material properties of investigated composites

	Y^C (MPa)	Y^T (MPa)	S^T (MPa)	$(\lvert\sigma_{22}^{Tran}\rvert, \lvert\tau_{23}^{Tran}\rvert)$ (MPa, MPa)
Melro et al. [18]	114.4	48.32	46.28	(26, 47)
Danial et al. [37]	115.5	51.47	42.67	(33.6,45.3)

6. Conclusions

In this paper, a comprehensive set of computational micromechanics RVE models have been developed to investigate the failure mechanisms and failure envelopes of UD CFRP composites under multi-axial stress states. We first compare the failure envelopes obtained from the computational models with classical failure criteria. The results indicate that in the σ_{22}-τ_{12} and σ_{22}-τ_{23} stress space, all the failure criteria fail to give satisfactory results for combined loading conditions in the regime of $\sigma_{22} \leqslant 0$, especially with the presence of high shear stress. For the stress space that involves fiber longitudinal compressive deformation, i.e., σ_{11}-τ_{12}, different failure criteria provide different predictions, and none of them shows quantitative agreement with our computational results. To overcome the limitations of the current failure criteria, a new set of homogenized failure criteria for the UD CFRP composites studied herein have been proposed based on the transitions of failure mechanisms observed from our computational micromechanics model. The proposed failure criteria have been validated with our computational and experimental results. In addition, we have compared the failure criteria with other experimental and numerical data found in the literature, good agreements between them are generally observed.

In conclusion, we have presented a thorough analysis of the failure criteria of UD CFRP composites by combining computational, theoretical, and experimental investigations. The analyses and methods presented in this study provide valuable solutions to the great challenge of failure prediction for composites used in structural applications. The workflow herein would also be generally applicable to formulate better failure criteria for other fiber reinforced composites.

Acknowledgments

The authors acknowledge the support from the Ford Motor Company with funding from the U.S. Department of Energy's Office of Energy Efficiency and Renewable Energy (EERE), under Award Number DE-EE0006867. In addition, the authors acknowledge the support from the Department of Civil and Environmental

Engineering and Mechanical Engineering at Northwestern University. Q.S. also acknowledges the support from the China Scholarship Council (CSC).

References

[1]. Totry E, González C, LLorca J. Failure locus of fiber-reinforced composites under transverse compression and out-of-plane shear. Composites Science and Technology. 2008;68(3-4):829-39.
[2]. Hinton MJ, Kaddour AS, Soden PD. Failure criteria in fibre reinforced polymer composites: the world-wide failure exercise: Elsevier; 2004.
[3]. Hart-Smith L. Predictions of the original and truncated maximum-strain failure models for certain fibrous composite laminates. Composites Science and Technology. 1998;58(7):1151-78.
[4]. Christensen R. Stress based yield/failure criteria for fiber composites. International journal of solids and structures. 1997;34(5):529-43.
[5]. Liu K-S, Tsai SW. A progressive quadratic failure criterion for a laminate1. Composites Science and Technology. 1998;58(7):1023-32.
[6]. Sun C, Tao J. Prediction of failure envelopes and stress/strain behaviour of composite laminates1. Composites Science and technology. 1998;58(7):1125-36.
[7]. Sun C, Tao J. Prediction of failure envelopes and stress/strain behavior of composite laminates. Failure Criteria in Fibre-Reinforced-Polymer Composites: Elsevier; 2004. p. 316-33.
[8]. Kuraishi A, Tsai SW, Liu KK. A progressive quadratic failure criterion, part B. Failure Criteria in Fibre-Reinforced-Polymer Composites: Elsevier; 2004. p. 903-21.
[9]. Hashin Z. Failure criteria for unidirectional fiber composites. Journal of applied mechanics. 1980;47(2):329-34.
[10]. Puck A, Schürmann H. Failure analysis of FRP laminates by means of physically based phenomenological models. Failure Criteria in Fibre-Reinforced-Polymer Composites: Elsevier; 2004. p. 832-76.
[11]. Pinho S, Iannucci L, Robinson P. Physically-based failure models and criteria for laminated fibre-reinforced composites with emphasis on fibre kinking: Part I: Development. Composites Part A: Applied Science and Manufacturing. 2006;37(1):63-73.
[12]. Pinho ST, Dàvila CG, Camanho PP, Iannucci L, Robinson P. Failure models and criteria for FRP under in-plane or three-dimensional stress states including shear non-linearity. 2005.
[13]. Davila C, Jaunky N, Goswami S, editors. Failure criteria for FRP laminates in plane stress. 44th AIAA/ASME/ASCE/AHS/ASC Structures, Structural Dynamics, and Materials Conference; 2003.
[14]. Cuntze R, Freund A. The predictive capability of failure mode concept-based strength criteria for multidirectional laminates. Composites Science and Technology. 2004;64(3-4):343-77.
[15]. Davila CG, Camanho PP, Rose CA. Failure criteria for FRP laminates. Journal of Composite materials. 2005;39(4):323-45.
[16]. Catalanotti G, Camanho P, Marques A. Three-dimensional failure criteria for fiber-reinforced laminates. Composite Structures. 2013;95:63-79.
[17]. Daniel IM, Daniel SM, Fenner JS. A new yield and failure theory for composite materials under static and dynamic loading. International Journal of Solids and Structures. 2017.

[18]. Camanho P, Arteiro A, Melro A, Catalanotti G, Vogler M. Three-dimensional invariant-based failure criteria for fibre-reinforced composites. International Journal of Solids and Structures. 2015;55:92-107.
[19]. Maimí P, Camanho PP, Mayugo J, Dávila C. A continuum damage model for composite laminates: Part I–Constitutive model. Mechanics of Materials. 2007;39(10):897-908.
[20]. Shahabi E, Forouzan MR. A damage mechanics based failure criterion for fiber reinforced polymers. Composites Science and Technology. 2017;140:23-9.
[21]. Soden P, Hinton M, Kaddour A. A comparison of the predictive capabilities of current failure theories for composite laminates. Composites Science and Technology. 1998;58(7):1225-54.
[22]. Kaddour A, Hinton M, Soden P. A comparison of the predictive capabilities of current failure theories for composite laminates: additional contributions. Composites Science and Technology. 2004;64(3-4):449-76.
[23]. Vaughan T, McCarthy C. Micromechanical modelling of the transverse damage behaviour in fibre reinforced composites. Composites Science and Technology. 2011;71(3):388-96.
[24]. Canal LP, Segurado J, LLorca J. Failure surface of epoxy-modified fiber-reinforced composites under transverse tension and out-of-plane shear. International journal of solids and structures. 2009;46(11-12):2265-74.
[25]. Totry E, González C, LLorca J. Prediction of the failure locus of C/PEEK composites under transverse compression and longitudinal shear through computational micromechanics. Composites Science and Technology. 2008;68(15-16):3128-36.
[26]. Romanowicz M. A numerical approach for predicting the failure locus of fiber reinforced composites under combined transverse compression and axial tension. Computational Materials Science. 2012;51(1):7-12.
[27]. Vogler T, Hsu S-Y, Kyriakides S. Composite failure under combined compression and shear. International Journal of Solids and Structures. 2000;37(12):1765-91.
[28]. Naya F, González C, Lopes C, Van der Veen S, Pons F. Computational micromechanics of the transverse and shear behavior of unidirectional fiber reinforced polymers including environmental effects. Composites Part A: Applied Science and Manufacturing. 2017;92:146-57.
[29]. Vajari DA. A micromechanical study of porous composites under longitudinal shear and transverse normal loading. Composite Structures. 2015;125:266-76.
[30]. Sun Q, Meng Z, Zhou G, Lin S-P, Kang H, Keten S, et al. Multi-Scale Computational Analysis of Unidirectional Carbon Fiber Reinforced Polymer Composites under Various Loading Conditions. Composite Structures. 2018;196:30-43.
[31]. Herráez M, González C, Lopes C, de Villoria RG, LLorca J, Varela T, et al. Computational micromechanics evaluation of the effect of fibre shape on the transverse strength of unidirectional composites: an approach to virtual materials design. Composites Part A: Applied Science and Manufacturing. 2016;91:484-92.
[32]. Pathan M, Tagarielli V, Patsias S. Effect of fibre shape and interphase on the anisotropic viscoelastic response of fibre composites. Composite Structures. 2017;162:156-63.
[33]. Sun Q, Guo H, Zhou G, Meng Z, Kang H, Keten S, et al. Experimental and Computational Analysis of Failure Mechanisms in Unidirectional Carbon Fiber Reinforced Polymer Laminates under Longitudinal Compression Loading. Composite Structures. 2018;203:335-48.

[34]. Vaughan T, McCarthy C. A micromechanical study on the effect of intra-ply properties on transverse shear fracture in fibre reinforced composites. Composites Part A: Applied Science and Manufacturing. 2011;42(9):1217-28.
[35]. Totry E, Molina-Aldareguía JM, González C, LLorca J. Effect of fiber, matrix and interface properties on the in-plane shear deformation of carbon-fiber reinforced composites. Composites Science and Technology. 2010;70(6):970-80.
[36]. Danzi F, Fanteria D, Panettieri E, Palermo M. A numerical micro-mechanical study of the influence of fiber–matrix interphase failure on carbon/epoxy material properties. Composite Structures. 2017;159:625-35.
[37]. Vajari DA, González C, Llorca J, Legarth BN. A numerical study of the influence of microvoids in the transverse mechanical response of unidirectional composites. Composites Science and Technology. 2014;97:46-54.
[38]. Melro A, Camanho P, Pinho S. Generation of random distribution of fibres in long-fibre reinforced composites. Composites Science and Technology. 2008;68(9):2092-102.
[39]. Galli M, Botsis J, Janczak-Rusch J. An elastoplastic three-dimensional homogenization model for particle reinforced composites. Computational Materials Science. 2008;41(3):312-21.
[40]. Sadowski T, Nowicki T. Numerical investigation of local mechanical properties of WC/Co composite. Computational Materials Science. 2008;43(1):235-41.
[41]. Hibbitt, Karlsson, Sorensen. ABAQUS/Explicit: user's manual: Hibbitt, Karlsson and Sorenson Incorporated; 2001.
[42]. Sádaba S HM, Naya F, et al. Special-purpose elements to impose Periodic Boundary Conditions for multiscale computational homogenization of composite materials with the explicit Finite Element Method. Composite Structures. 2019;208:434-41.
[43]. Kanit T, Forest S, Galliet I, Mounoury V, Jeulin D. Determination of the size of the representative volume element for random composites: statistical and numerical approach. International Journal of solids and structures. 2003;40(13-14):3647-79.
[44]. Pahr D, Böhm H. Assessment of mixed uniform boundary conditions for predicting the mechanical behavior of elastic and inelastic discontinuously reinforced composites. Comput Model Engng Sci. 2008;34:117-36.
[45]. Chen G, Ozden U, Bezold A, Broeckmann C. A statistics based numerical investigation on the prediction of elasto-plastic behavior of WC–Co hard metal. Computational Materials Science. 2013;80:96-103.
[46]. González C, LLorca J. Mechanical behavior of unidirectional fiber-reinforced polymers under transverse compression: microscopic mechanisms and modeling. Composites Science and Technology. 2007;67(13):2795-806.
[47]. Ducobu F R-LE, Filippi E. On the introduction of adaptive mass scaling in a finite element model of Ti6Al4V orthogonal cutting. Simulation Modelling Practice and Theory. 2015;53:1-14.
[48]. Melro A, Camanho P, Pires FA, Pinho S. Micromechanical analysis of polymer composites reinforced by unidirectional fibres: Part I–Constitutive modelling. International Journal of Solids and Structures. 2013;50(11-12):1897-905.
[49]. Liu P, Li X. A Large-scale Finite Element Model on Micromechanical Damage and Failure of Carbon Fiber/Epoxy Composites Including Thermal Residual Stress. Applied Composite Materials. 2018;25(3):545-60.

[50]. Liu P, Xing L, Zheng J. Failure analysis of carbon fiber/epoxy composite cylindrical laminates using explicit finite element method. Composites Part B: Engineering. 2014;56:54-61.
[51]. Meng Z, Bessa MA, Xia W, Kam Liu W, Keten S. Predicting the macroscopic fracture energy of epoxy resins from atomistic molecular simulations. Macromolecules. 2016;49(24):9474-83.
[52]. Kenane M, Benzeggagh M. Mixed-mode delamination fracture toughness of unidirectional glass/epoxy composites under fatigue loading. Composites Science and Technology. 1997;57(5):597-605.
[53]. Vogler T, Kyriakides S. Inelastic behavior of an AS4/PEEK composite under combined transverse compression and shear. Part I: experiments. International Journal of Plasticity. 1999;15(8):783-806.
[54]. Totry E, González C, LLorca J. Influence of the loading path on the strength of fiber-reinforced composites subjected to transverse compression and shear. International journal of solids and structures. 2008;45(6):1663-75.
[55]. Pinho S, Darvizeh R, Robinson P, Schuecker C, Camanho P. Material and structural response of polymer-matrix fibre-reinforced composites. Journal of Composite Materials. 2012;46(19-20):2313-41.
[56]. Gutkin R, Pinho S, Robinson P, Curtis P. Micro-mechanical modelling of shear-driven fibre compressive failure and of fibre kinking for failure envelope generation in CFRP laminates. Composites Science and Technology. 2010;70(8):1214-22.
[57]. Bai X, Bessa MA, Melro AR, Camanho PP, Guo L, Liu WK. High-fidelity micro-scale modeling of the thermo-visco-plastic behavior of carbon fiber polymer matrix composites. Composite Structures. 2015;134:132-41.
[58]. Vogler T, Hsu S-Y, Kyriakides S. On the initiation and growth of kink bands in fiber composites. Part II: analysis. International Journal of Solids and Structures. 2001;38(15):2653-82.
[59]. Kyriakides S, Arseculeratne R, Perry E, Liechti K. On the compressive failure of fiber reinforced composites. International Journal of Solids and Structures. 1995;32(6-7):689-738.
[60].Yurgartis S. Measurement of small angle fiber misalignments in continuous fiber composites. Composites Science and Technology. 1987;30(4):279-93.
[61].Pimenta S, Gutkin R, Pinho S, Robinson P. A micromechanical model for kink-band formation: Part II—Analytical modelling. Composites Science and Technology. 2009;69(7-8):956-64.
[62]. Gutkin R, Pinho S, Robinson P, Curtis P. A finite fracture mechanics formulation to predict fibre kinking and splitting in CFRP under combined longitudinal compression and in-plane shear. Mechanics of Materials. 2011;43(11):730-9.
[63]. Liu K-S, Tsai SW. A progressive quadratic failure criterion for a laminate. Failure Criteria in Fibre-Reinforced-Polymer Composites: Elsevier; 2004. p. 334-52.
[64]. Hill R. Theory of mechanical properties of fibre-strengthened materials: I. Elastic behaviour. Journal of the Mechanics and Physics of Solids. 1964;12(4):199-212.
[65]. Hashin Z, Rotem A. A fatigue failure criterion for fiber reinforced materials. Journal of composite materials. 1973;7(4):448-64.
[66]. Daniel IM. Yield and failure criteria for composite materials under static and dynamic loading. Progress in Aerospace Sciences. 2016;81:18-25.
[67]. Dvorak GJ, Laws N. Analysis of progressive matrix cracking in composite laminates II. First ply failure. Journal of Composite Materials. 1987;21(4):309-29.

[68]. Edge E. Stress-based grant-sanders method for predicting failure of composite laminates. Composites Science and Technology. 1998;58(7):1033-41.
[69]. Puck A, Kopp J, Knops M. Guidelines for the determination of the parameters in Puck's action plane strength criterion. Composites Science and Technology. 2002;62(3):371-8.
[70]. Chowdhury NT, Wang J, Chiu WK, Yan W. Matrix failure in composite laminates under compressive loading. Composites Part A: Applied Science and Manufacturing. 2016;84:103-13.
[71]. Chowdhury NT, Wang J, Chiu WK, Yan W. Matrix failure in composite laminates under tensile loading. Composite Structures. 2016;135:61-73.
[72]. Daniel I, Werner B, Fenner J. Strain-rate-dependent failure criteria for composites. Composites Science and Technology. 2011;71(3):357-64.
[73]. Gan KW, Laux T, Taher ST, Dulieu-Barton JM, Thomsen OT. A novel fixture for determining the tension/compression-shear failure envelope of multidirectional composite laminates. Composite Structures. 2018;184:662-73.
[74]. Pinho ST. Modelling failure of laminated composites using physically-based failure models. 2005.
[75]. Pinho ST, Davila CG, Camanho PP, Iannucci L, Robinson P. Failure models and criteria for FRP under in-plane or three-dimensional stress states including shear non-linearity. 2005.
[76]. Yerramalli CS, Waas AM. A failure criterion for fiber reinforced polymer composites under combined compression–torsion loading. International journal of solids and structures. 2003;40(5):1139-64.
[77]. Michaeli W, Mannigel M, Preller F. On the effect of shear stresses on the fibre failure behaviour in CFRP. Composites Science and Technology. 2009;69(9):1354-7.
[78]. Soden P, Hinton M, Kaddour A. Biaxial test results for strength and deformation of a range of E-glass and carbon fibre reinforced composite laminates: failure exercise benchmark data. Failure Criteria in Fibre-Reinforced-Polymer Composites: Elsevier; 2004. p. 52-96.